Title:

An online, energy-resolving beam profile detector for laser-driven proton beams

Authors:

J. Metzkes, K. Zeil, S. D. Kraft, L. Karsch, M. Sobiella, M. Rehwald, L. Obst, H.-P. Schlenvoigt, U. Schramm

Final manuscript

The original publication may be found at:

Journal: Review of Scientific Instruments 87, 083310 (2016)

DOI: http://dx.doi.org/10.1063/1.4961576

An online, energy-resolving beam profile detector for laser-driven proton beams

J. Metzkes[1,2], K. Zeil[1], S. D. Kraft[1], L. Karsch[3], M. Sobiella[1], M. Rehwald[1,2], L. Obst[1,2], H.-P. Schlenvoigt[1], U. Schramm[1,2]

[1]Helmholtz-Zentrum Dresden – Rossendorf (HZDR), Bautzner Landstr. 400, 01328 Dresden, Germany

[2]Technische Universität Dresden, 01062 Dresden, Germany

[3]OncoRay-National Center for Radiation Research in Oncology, Technische Universität Dresden, 01307 Dresden, Germany

Abstract. In this paper, a scintillator-based online beam profile detector for the characterization of laser-driven proton beams is presented. Using a pixelated matrix with varying absorber thicknesses, the proton beam is spatially resolved in two dimensions and simultaneously energy-resolved. A thin plastic scintillator placed behind the absorber and read out by a CCD camera is used as the active detector material. The spatial detector resolution reaches down to $\sim 4\,\mathrm{mm}$ and the detector can resolve proton beam profiles for up to 9 proton threshold energies. With these detector design parameters, the spatial characteristics of the proton distribution and its cut-off energy can be analyzed online and on-shot under vacuum conditions. The paper discusses the detector design, its characterization and calibration at a conventional proton source as well as the first detector application at a laser-driven proton source.

1. Introduction

Laser-driven ion sources (LDIS) exploit the extremely high electric fields of $\sim$TV/m amplitude which can be sustained in over-critical laser-produced plasmas. These fields serve the acceleration of protons and heavier ions, which mainly originate from the hydro-carbon contaminant layer and which gain kinetic energies of several 10 MeV per nucleon on micrometer spatial scales (e.g. [1]). Owing to the spatial compactness of the acceleration, combined with a high particle flux, a short particle pulse duration and a high beam laminarity [2], LDIS are potentially advantageous for numerous applications ([1] and therein), as e.g. ion/proton radiation therapy of cancer [3].

The development of applicable LDIS and the realization of first application experiments (e.g. [4, 5, 6, 7]) hinges among other factors on the provision of online diagnostic tools adapted to the properties of laser-accelerated ion and proton pulses. Among others, these features are exponentially decreasing energy spectra with cut-off energies of up to currently several 10 MeV for the class of application-relevant high-power, ultra-short pulse (τ of several 10 fs) laser sources [8, 9, 10]. The particle emission from the non-irradiated target surface occurs within an angle of $\sim 20^\circ$ (half angle) around the target normal direction ([1] and therein). The cut-off energy of the spectrum is used as a benchmark for the acceleration performance, whereas the spatial emission pattern can carry information about e.g. the target surface [11, 2] or the spatio-temporal properties of the laser pulse [12].

Due to the large energy range as well as emission angle of the multi-species pulses from LDIS, a combination of detection methods is commonly used in experimental setups: Thomson parabola spectrometers (TPS) provide spectra with high energy resolution on the percent level [13] for all ion species accelerated in the interaction but only probe a small fraction (0.02 µsr) out of the beam's solid angle. Read-out by microchannel plate

detectors, scintillators or pixel detectors [14], TPS allow for the online characterization of the particle energy distribution at the $\sim$Hz repetition rate of application-relevant high-power laser sources.

For protons, absolutely calibrated area detectors such as self-developing radiochromic films (RCF) [15, 16] or nuclear activation imaging (NAIS) [17] serve as complementatary tools which provide the proton number and spatial distribution of the accelerated proton pulse[**?**, **?**, **?**]. From stacks of e.g. RCF, the spatially resolved spectrum can be deconvoluted from the depth dose profile via the energy-range-correlation of the protons in the material [15, 16, 17]. The energy resolution is $\sim 1\,\mathrm{MeV}$. However, both RCF and NAIS are offline methods which require the extraction of the detector from the vacuum chamber in which the experiment is performed.

This shortcoming is overcome by a class of online area detectors which - as RCF or NAIS - use the energy-range-correlation of protons in an absorber to yield energy resolution and rely on plastic scintillators read out by a CCD camera as detector material [18, 19]. In the case of the area detector developed by Green *et al.*, for instance, the proton beam profile in two dimensions for three different threshold energies is derived from a stack of three plastic scintillators which emit at different wavelength [18]. This approach, in which the scintillators function as absorber as well as active detector material, yields a high spatial but low energy resolution.

For the compact scintillator-based online area detector presented in this paper, the number of resolvable threshold energies is increased and made scalable through the use of a separate aluminum absorber plate in front of a single scintillator layer. The absorber plate is segmented into 60 macro-pixels, each resolving up to 9 different threshold energies by the use of different absorber thicknesses. This approach reduces the spatial detector resolution to $4\,\mathrm{mm} \times 4\,\mathrm{mm}$ (smallest macro-pixel size) but it is optimized to

provide the energy-dependent proton beam spot size together with the cut-off energy of the spectrum. The absolute proton number calibration of the detector can facilitate the reconstruction of the proton distribution as performed in RCF spectroscopy [15, 16].

The paper is structured as follows: In Sec. 2, the detector principle and setup are presented in detail, followed by results of the detector characterization and calibration at a conventional proton source. Sec. 3 summarizes the results of the first detector application at a LDIS.

2. Detector Design, Optimization and Characterization

2.1. Detector Principle

The setup of the scintillator-based 2D pixel detector, as shown in Fig. 1a, comprises of a detector unit and a CCD camera unit (compare [19]). The central part of the detector unit is the 48 mm × 48 mm large absorber matrix machined into a 2.5 mm thick aluminum plate. Designed for a location of about 50 mm behind the target, the detector's field of view has a half-angle of 26° with respect to the proton (point) source and can therefore record a two-dimensional imprint of the entire proton beam. The absorber plate is segmented into 60 macro-pixels, each containing 3, 9 or 16 holes countersunk into the aluminum plate (Fig. 1b). These countersunk holes will be referred to *absorber holes* in the following. To provide for energy resolution, the depths of the countersunk holes are varied so that different remaining aluminum absorber thicknesses are obtained within each macro-pixel. Placed into the proton beam, protons which are energetic enough to pass the aluminum thickness of a specific absorber hole, deposit energy in the 200 µm thick layer of polyvinyltoluene-based plastic scintillator BC416 (Bicron) behind the aluminum plate. The energy deposition excites the emission of scintillation photons at 434 nm, which is imaged onto a CCD camera. A representative raw data image is

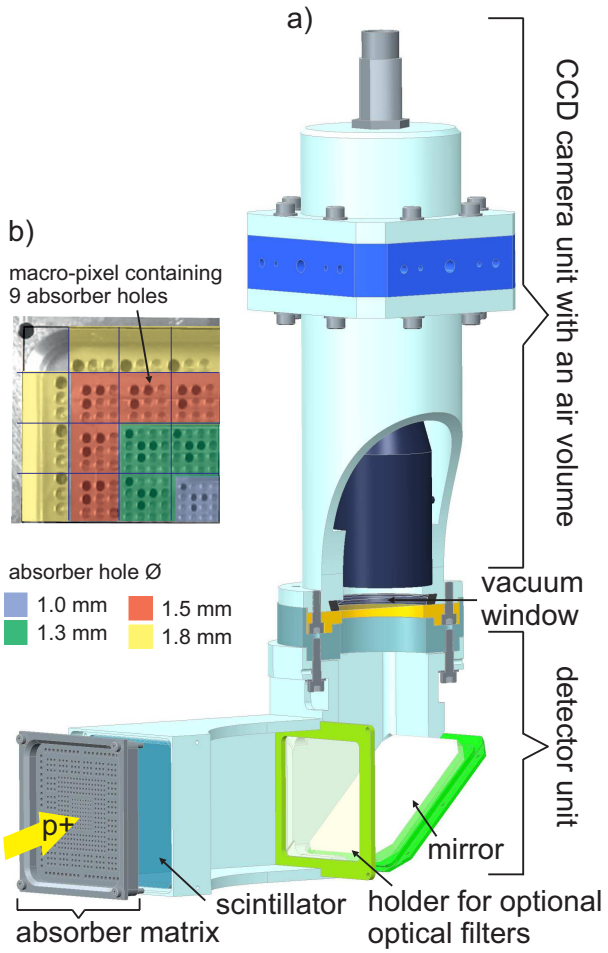

c) Proton threshold energies for the final design

absorber thickness [µm]	threshold energy [MeV]
0	0
250	5.9
450	8.2
650	10.2
850	11.9
1150	14.1
1450	16.1
1800	18.2
2150	20.1

d) Proton threshold energies for the prototype design

absorber thickness [µm]	threshold energy [MeV]
0	0
300	6.5
400	7.7
500	8.8
600	9.7
700	10.6
800	11.4

Figure 1. Setup of the 2D pixel detector. a) Technical drawing. b) Photograph of the upper-left quadrant of the absorber matrix. The different macro-pixels are separated by purple lines and the different zones of absorber hole diameters are color-coded. The other three quadrants are filled by rotating the shown quadrant by 90°, 180° and 270° around its lower-right corner. In that way, the absorber matrix is invariant to rotations, which simplifies the setup. c - d) Absorber thicknesses in the absorber matrix and the according proton threshold energies for the final design optimized for the application at LDIS and the prototype design, for which data are presented in this paper. Data source: [20].

shown in Fig. 2. Each of the bright spots corresponds to an absorber hole and represents the signal from protons above a minimum kinetic energy (i.e. proton threshold energy), which is given by the proton energy-range-correlation for the specific absorber thickness. Each macro-pixel hence samples a specific part of the beam and resolves up to 9‡ proton

‡ For detector characterization experiments at the 6 MV Van de Graaff tandetron accelerator at the Helmholtz-Zentrum Dresden - Rossendorf (HZDR) and first experiments at a LDIS, a prototype detector design with specifically adapted absorber thicknesses was used (Fig. 1d).

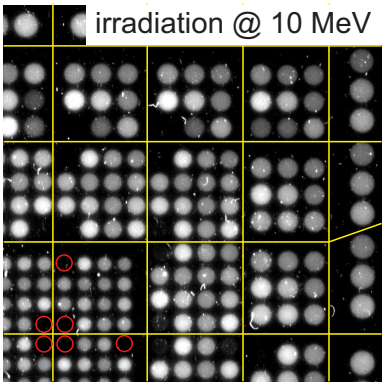

Figure 2. Representative raw data of the 2D pixel detector. The detector was irradiated with 10 MeV protons at the HZDR tandetron accelerator. The individual macro-pixels are marked by yellow lines. The scintillator signal increases from black to white in the color scale of the image. The absorber holes with the brightest signal are those where the proton's Bragg peak lies in the scintillator layer. On the other hand, in accordance with a range of 630 µm [20] in aluminum for 10 MeV protons, the absorber holes for 800 µm absorber thickness are dark (exemplarily marked with red circles for the central macro-pixels).

threshold energies in the final detector design for LDIS. The absorber thicknesses and according threshold energies are summarized in Fig. 1c.

The imaging of the scintillator is performed with a 25 mm focal length objective and an AVT GUPPY PRO F-201B CCD camera, yielding an image resolution of 41 µm/pixel or 24 px/mm. Camera and objective are housed in the CCD camera unit (Fig. 1a). This unit contains a small air volume of $\sim$0.5 l to cool the camera in the otherwise evacuated experimental chamber (compare [19]). In this way, the compact detector with a footprint of only 60 mm $\times$ 160 mm and a height of 320 mm can be positioned close to the laser-target-interaction point without having to set up an optical beam path out of the experimental chamber.

To avoid that the camera chip is directly exposed to radiation, a mirror placed at an angle of 45° folds the optical beam path so that the CCD chip is oriented horizontally with respect to the proton beam and sits above the proton beam axis.

2.2. Experimental Optimization of the Absorber Matrix Parameters

The absorber matrix principle, as sketched above, leaves the absorber hole diameters and the absorber hole spacing as design parameters. Both parameters are favorably kept small to increase the spatial resolution of the detector. A lower limit is however set by the requirement of an evaluable detector signal, which demands that the background signal caused by protons scattered in the absorber hole walls and caused by cross-talk between neighboring absorber holes is suppressed. Proton scattering is particularly relevant for absorber holes off-center on the absorber matrix, where the angle between the incoming proton beam (originating from a point source) and the absorber hole axis is increased.

The optimal choice for these geometric absorber matrix parameters was experimentally investigated at the 6 MV Van de Graaff tandetron accelerator at the Helmholtz-Zentrum Dresden – Rossendorf (HZDR) using two different test absorber matrices. The first absorber matrix was designed to optimize the absorber hole diameter, thereby including the influence of proton scattering. It featured absorber hole diameters ranging from 0.5 - 2.5 mm. In order to mimic the scattering effects of the divergent beam at LDIS in the case of the parallel beam at the tandetron accelerator, the absorber holes were machined with orientations of 0°, 5°, 15° and 30° with respect to the proton beam axis. On a second absorber matrix, the absorber hole distance was varied in the range of 0.5 - 1.25 mm in steps of 0.25 mm in order to find the optimal absorber hole spacing. Spacing here refers to the minimal width of material between two absorber holes and not the center-to-center distance. The absorber hole diameter was set to 1 mm for the spacing of 0.5 mm and to 1.5 mm for all other cases.

Both plates were irradiated at a proton energy of 11.8 MeV. The proton beam spot from the accelerator was adapted to the absorber matrix size by beam scanning. For post-

processing, the camera signal of each signal spot (corresponding to an absorber hole) was averaged over a circular ROI with 50% of the nominal absorber hole diameter. Comparison of different ROI sizes showed that for a 50% ROI the mean signal deviates by less than 5% from the average over the signal spot center (25% ROI) for all absorber hole diameters, rendering a 50% ROI standard for data evaluation. Fig. 3 summarizes the results for the absorber hole diameter and orientation scan, showing that the camera signal is almost independent from the absorber hole diameter down to 1.5 mm and decreases by 14% for a diameter of 1.0 mm. A further reduction of the absorber hole diameter, e.g. down to 0.5 mm, can according to the data not be recommended, since scattering leads to a strong signal reduction.

The relative orientation between absorber hole axis and incoming proton beam has no influence on the signal for the chosen ROI size of 50% (Fig. 3). Therefore, the absorber holes are oriented normally to the absorber matrix surface in the prototype and final design of the detector. The effect that the absorber holes located off-center on the detector surface are irradiated under an angle (proton point source) and hence feature a reduced solid angle of detection, is compensated for by increasing the absorber hole diameter from 1 mm in the detector center to 1.8 mm towards the detector edge (Fig. 1b). In principle, the grazing incidence under an angle α onto the absorber matrix at off-center positions also influences the energy of protons reaching the scintillator as protons then pass an increased absorber thickness. Amounting to less than 10% in thickness gain, this effect can however be neglected for most practical purposes.

For the distance of neighboring absorber holes, the optimum value was determined to 0.5 mm. That provides well-separated signal spots on the CCD camera image (see Fig. 2), which simplifies the automatic readout for subsequent data analysis. The yielded optimum distance is in good agreement with the fact that a localized energy deposition at

the scintillator front surface is expected to result in a scintillation spot with a diameter of 330 µm at the rear surface of the 200 µm thick scintillator layer due to the critical angle of $\theta_c = 39.3°$ for total internal reflection in the scintillator material. Hence, crosstalk between neighboring absorber holes is suppressed apart from protons scattering in the material.

In summary, the prototype and final design of the detector feature a macro-pixel size and hence spatial resolution of 4 mm × 4 mm in the detector center. Within this macro-pixel, up to 7/9 threshold energies can be resolved (prototype/final design). The energy resolution can flexibly be chosen via the absorber thicknesses and is ultimately limited by the scintillator thickness.

2.3. Proton Number Calibration of the Detector

For the absolute calibration of the CCD camera signal per proton passing through the scintillator, the absorber matrix shown in Fig. 1b was replaced by an aluminum plate with a 20 mm large aperture in the center, behind which a 13 µm thick light-tight plastic foil (Pokalon®) and the 200 µm thick scintillator were placed. The diameter of the proton beam was reduced to 10 mm in order to exclude the influence of proton scattering at the aluminum absorber plate on the measurement. The calibration was performed at a proton energy of 7 MeV from the tandetron accelerator, which corresponds to a differential energy deposition of $dE/dx = (7.0 \pm 0.3)$ keV/µm in the scintillator. The resulting camera signal per proton rescaled to a camera gain of 0 is (0.45 ± 0.01) counts. When estimating the radiation dose or particle number for the spectrally broad proton pulses from LDIS based on the presented calibration, the nonlinear light yield of plastic scintillators as a function of the differential energy deposition dE/dx (ionization quenching [21]) has in principle to be taken into account. However, for all practical purposes at current LDIS (proton energy spectra in the range of 2 - 40 MeV), a proton

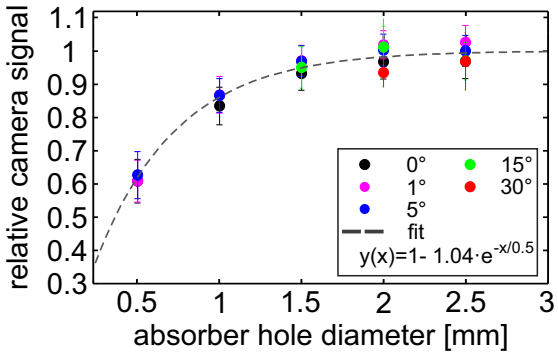

Figure 3. Optimization of the absorber matrix parameters. Relative camera signal (normalized to an absorber hole diameter $d \to \infty$ based on the fit) as a function of the absorber hole diameter and the irradiation angle. Each data point represents the average over 20 (10 for 30° orientation) absorber holes and the error bars include the standard deviation of the ROI as well as the sample mean. The absorber hole orientation of 30° was only tested for the large absorber hole diameters as the sight through the hole is otherwise blocked. The relative camera signal for an arbitrary absorber hole diameter can be calculated via the fitted exponential recovery function.

number estimated using the above-given calibration is correct within a factor of two.

3. Application at a Laser-Based Accelerator

The detector prototype was tested at the 150 TW Draco laser facility at the HZDR [22, 12]. The applied 30 fs long laser pulse had a maximum pulse energy (E_L) of 3.8 J on target and was focused to a spot diameter of 3 µm (FWHM). In the interaction with a 5 µm thick titanium foil, protons with exponential spectra and cut-off energies of $\sim$11 - 13 MeV were yielded, as verified by RCF§ and Thomson parabola spectrometer‖ measurements.

The scintillator-based detector was placed $\sim$50 mm behind the proton-emitting target and could hence capture the entire proton beam. In addition to the absorber matrix, 13 µm of aluminum were placed in front of the scintillator to shield the detector from laser light. Representative raw data are shown in Fig. 4a. In contrast to the raw data taken with the collimated proton beam from the tandetron accelerator (Fig. 2), the

§ proton cut-off energy between 10.6 MeV and 12 MeV
‖ proton cut-off energy between 11 MeV and 13 MeV

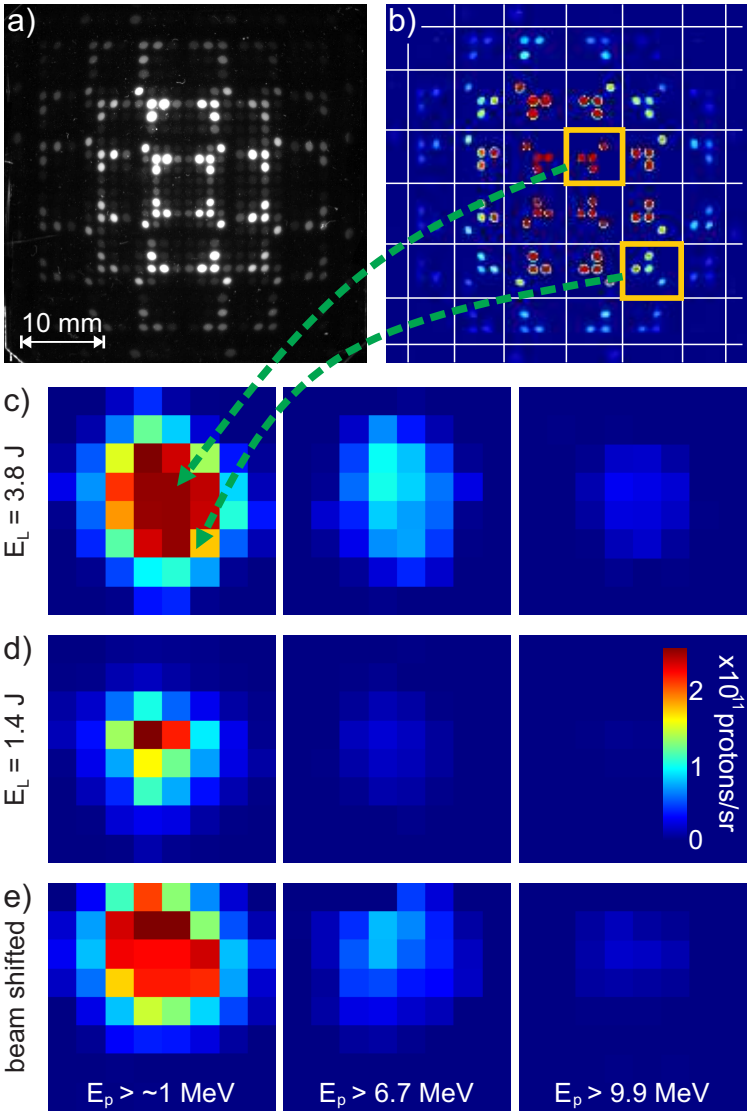

Figure 4. Detector application at the 150 TW Draco laser facility. a) Raw data image of the scintillator applied at a LDIS. The scintillator signal increases from black to white. b) False-color image of a) showing only absorber holes with an absorber thickness of 13 µm, i.e. the aluminum layer placed in front of the scintillator as a light shield. The white lines represent the macro-pixels of the detector surface and the arrows indicate the macro-pixel redistribution in the final evaluated detector output. The final detector signal for one marco-pixel and specific threshold energy is derived by averaging over all signal spots within one macro-pixel that correspond to the same absorber thickness (i.e. four signal spots in the given examples). c) - e) Evaluated detector signals for three different proton source configurations (vertical direction). The detector signals correspond to the spatially resolved integrated number of protons above a proton threshold energy E_p, where E_p is given at the bottom of e) and increases from left to right from $\sim$ 1 MeV to 9.9 MeV.

distortion of the image caused by the point source laser-driven proton beam is clearly visible. The distortion is caused by protons which travel through the absorber holes

at an angle so that the resulting spot of light emission on the scintillator acquires an elliptical shape. The effect increases with the distance from the detector center but has no influence on the data evaluation.

The data extraction from the raw data images comprises two steps. At first, all absorber holes with the same absorber thickness are summarized in layers, as shown for the absorber thickness of 13 µm¶ in Fig. 4b. In a second step, the signal of each absorber hole is re-calculated to a proton number based on the calibration, before the signal of each absorber layer is reorganized into the macro-pixel pattern of the detector (green arrows in Fig. 4b/c).

In Fig. 4c - e, resulting experimental data for three different proton source configurations are compared. From c) to d), the laser energy was reduced by a factor of 2.6, the resulting decrease in the proton cut-off energy clearly being resolved by the detector. In Fig. 4e, the lateral distance between the center of the detector and the proton point source was shifted by 10 mm, which is resolved well by the shifted beam profile on the detector. For the given setup, a lateral shift by 10 mm is equivalent to an angle of $\sim 10°$. Hence, even though the spatial resolution of the macro-pixels is only in the range of millimeters, experimentally relevant angular shifts of the proton beam's center of mass can be measured [12].

4. Summary

In conclusion, the presented online detector system resolves the spatial profile of a laser-driven proton beam (4 mm spatial resolution in the central part of the detector) and it can distinguish up to 9 threshold energies. In that way, the detector can complement the established diagnostic tools of RCF and Thomson parabola spectrometers by providing

¶ This absorber thickness refers to the absorber holes with 0 µm remaining absorber thickness in the absorber matrix, which were then covered by a layer of aluminum for light protection, as described above.

online the maximum proton energy, the proton yield, the approximate energy-dependent proton beam size as well as the position of the beam's center of mass on a single-shot basis. Based on these parameters, the acceleration performance of the laser-plasma-based source can be monitored and optimized, which is a crucial point for a further development of laser-driven ion sources towards applicable particle sources. The compact detector size allows for the detector's integration in various experimental setups. The repetition rate of the detector is only limited by the capabilities of the CCD camera used in the detector and can cope with the at most $\sim$ Hz repetition rates of current high-power laser systems.

Due to its modular design regarding the absorber matrix (macro-pixel arrangement and absorber thickness), the detector can easily be adapted to different experimental requirements. To be used with the upcoming class of Petawatt laser sources, for which an increase in proton energies is expected, the absorber thicknesses can be increased accordingly. At the same time, the increased proton dose will allow to place the detector further away from the proton source, which automatically improves the spatial resolution of the proton beam. Moreover, the spatial resolution and the number of resolved threshold energies can be traded respectively by increasing or decreasing the number of absorber holes per macro-pixel and hence the macro-pixel size.

If the detector is applied in combination with a Thomson parabola spectrometer, an additional 3 mm large hole through the absorber matrix center, the scintillator and the mirror can be used to let the central part of the proton distribution pass into the spectrometer downstream. In order to shield the interior of the scintillator-based detector from light produced in the laser-target interaction, a thin metal tube is then inserted in the detector interior, connecting the hole in the absorber matrix center with the hole in the mirror. An according setup was successfully tested at the Draco

experimental setup.

An interesting extension of the 2D pixel detector can be achieved when using a transparent absorber matrix sandwiched in between two plastic scintillator layers emitting at two different wavelength (compare [18]). Whereas the absorber and second scintillator function as in the original design, the first scintillator additionally provides a spatially highly resolved 2D profile of the proton distribution. Both signals are separated using a color CCD camera.

5. Acknowledgements

We gratefully acknowledge the support from Dr. Shavkat Akhmadaliev and his team at the HZDR tandetron accelerator and from S. Bock, U. Helbig and R. Gebhardt at the Draco laser facility (HZDR). The work has been partially supported by EC Horizon 2020 LASERLAB-EUROPE/LEPP (contract 654148) and by the German Federal Ministry of Education and Research (BMBF) under contract number 03Z1O511.

6. References

[1] H. Daido, M. Nishiuchi, and A. S. Pirozhkov. Review of laser-driven ion sources and their applications. *Reports on Progress in Physics*, 75(5):056401, 2012.

[2] T. E. Cowan, J. Fuchs, H. Ruhl, A. Kemp, P. Audebert, M. Roth, R. Stephens, I. Barton, A. Blazevic, J. C. Gauthier, M. Geissel, M. Hegelich, J. Kaae, S. Karsch, G. P. Le Sage, S. Letzring, M. Manclossi, S. Meyroneinc, A. Newkirk, H. Pepin, N. Renard Legalloudec, and J. Ferna. Ultralow Emittance, Multi-MeV Proton Beams from a Laser Virtual-Cathode Plasma Accelerator. *Physical Review Letters*, 92(20):204801, 2004.

[3] S. V. Bulanov and V. S. Khoroshkov. Feasibility of using laser ion accelerators in proton therapy. *Plasma Physics Reports*, 28(5):453–456, 2001.

[4] M. Borghesi, A. Schiavi, D. H. Campbell, M. G. Haines, O. Willi, A. J. MacKinnon, L. A. Gizzi,

M. Galimberti, R. J. Clarke, and H. Ruhl. Proton imaging: a diagnostic for inertial confinement fusion/fast ignitor studies. *Plasma Physics and Controlled Fusion*, 43(12A):A267–A276, 2001.

[5] A. Yogo, K. Sato, M. Nishikino, M. Mori, T. Teshima, H. Numasaki, M. Murakami, Y. Demizu, S. Akagi, S. Nagayama, K. Ogura, A. Sagisaka, S. Orimo, M. Nishiuchi, A. S. Pirozhkov, M. Ikegami, M. Tampo, H. Sakaki, M. Suzuki, I. Daito, Y. Oishi, H. Sugiyama, H. Kiriyama, H. Okada, S. Kanazawa, S. Kondo, T. Shimomura, Y. Nakai, M. Tanoue, H. Sasao, D. Wakai, P. R. Bolton, and H. Daido. Application of laser-accelerated protons to the demonstration of DNA double-strand breaks in human cancer cells. *Applied Physics Letters*, 94(18):181502, 2009.

[6] S. D. Kraft, C. Richter, K. Zeil, M. Baumann, E. Beyreuther, S. Bock, M. Bussmann, T. E. Cowan, Y. Dammene, W. Enghardt, U. Helbig, L. Karsch, T. Kluge, L. Laschinsky, E. Lessmann, J. Metzkes, D. Naumburger, R. Sauerbrey, M. Schürer, M. Sobiella, J. Woithe, U. Schramm, and J. Pawelke. Dose-dependent biological damage of tumour cells by laser-accelerated proton beams. *New Journal of Physics*, 12(8):85003, 2010.

[7] S. Busold, A. Almomani, V. Bagnoud, W. Barth, S. Bedacht, A. Blažević, O. Boine-Frankenheim, C. Brabetz, T. Burris-Mog, T. E. Cowan, O. Deppert, M. Droba, H. Eickhoff, U. Eisenbarth, K. Harres, G. Hoffmeister, I. Hofmann, O. Jaeckel, R. Jaeger, M. Joost, S. Kraft, F. Kroll, M. Kaluza, O. Kester, Z. Lecz, T. Merz, F. Nürnberg, H. Al-Omari, A. Orzhekhovskaya, G. Paulus, J. Polz, U. Ratzinger, M. Roth, G. Schaumann, P. Schmidt, U. Schramm, G. Schreiber, D. Schumacher, T. Stoehlker, A. Tauschwitz, W. Vinzenz, F. Wagner, S. Yaramyshev, and B. Zielbauer. Shaping laser accelerated ions for future applications - The LIGHT collaboration. *Nuclear Instruments and Methods in Physics Research, Section A: Accelerators, Spectrometers, Detectors and Associated Equipment*, 740:94–98, 2014.

[8] K. Ogura, M. Nishiuchi, A. S. Pirozhkov, T. Tanimoto, A. Sagisaka, T. Zh. Esirkepov, M. Kando, T. Shizuma, T. Hayakawa, H. Kiriyama, T. Shimomura, S. Kondo, S. Kanazawa, Y. Nakai, H. Sasao, F. Sasao, Y. Fukuda, H. Sakaki, M. Kanasaki, A. Yogo, S. V. Bulanov, P. R. Bolton, and K. Kondo Proton acceleration to 40 MeV using a high intensity, high contrast optical parametric chirped-pulse amplification/Ti:sapphire hybrid laser system. *Opt. Lett.*, 37(14):2868–2870, 2012.

[9] J. S. Green, A. P. L. Robinson, N. Booth, D. C. Carroll, R. J. Dance, R. J. Gray, D. A. MacLellan, P. McKenna, C. D. Murphy, D. Rusby, and L. Wilson. High efficiency proton beam generation through target thickness control in femtosecond laser-plasma interactions. *Applied Physics Letters*, 104(21):214101, 2014.

[10] J. H. Bin, W. J. Ma, H. Y. Wang, M. J. V. Streeter, C. Kreuzer, D. Kiefer, M. Yeung, S. Cousens, P. S. Foster, B. Dromey, X. Q. Yan, R. Ramis, J. Meyer-ter Vehn, M. Zepf, and J. Schreiber. Ion Acceleration Using Relativistic Pulse Shaping in Near-Critical-Density Plasmas. *Physical Review Letters*, 115(6):064801, 2015.

[11] M. Roth, A. Blazevic, M. Geissel, T. Schlegel, T. E. Cowan, M. Allen, J. C. Gauthier, P. Audebert, J. Fuchs, J. Meyer-Ter-Vehn, M. Hegelich, S. Karsch, and A. Pukhov. Energetic ions generated by laser pulses: A detailed study on target properties. *Physical Review Special Topics - Accelerators and Beams*, 5(6):31–38, 2002.

[12] K. Zeil, J. Metzkes, T. Kluge, M. Bussmann, T. E. Cowan, S. D. Kraft, R. Sauerbrey, and U. Schramm. Direct observation of prompt pre-thermal laser ion sheath acceleration. *Nature Communications* 3, 874, 2012.

[13] D. Jung, R. Hörlein, D. Kiefer, S. Letzring, D. C. Gautier, U. Schramm, C. Hübsch, R. Öm, B. J. Albright, J. C. Fernandez, D. Habs, and B. M. Hegelich. Development of a high resolution and high dispersion Thomson parabola. *Review of Scientific Instruments*, 82(1), 2011.

[14] S. Reinhardt, W. Draxinger, J. Schreiber, and W. Assmann. A pixel detector system for laser-accelerated ion detection. *Journal of Instrumentation*, 8(03):P03008–P03008, mar 2013.

[15] E. Breschi, M. Borghesi, M. Galimberti, D. Giulietti, L. A. Gizzi, and L. Romagnani. A new algorithm for spectral and spatial reconstruction of proton beams from dosimetric measurements. *Nuclear Instruments and Methods in Physics Research, Section A: Accelerators, Spectrometers, Detectors and Associated Equipment*, 522:190–195, 2004.

[16] F. Nürnberg, M. Schollmeier, E. Brambrink, A. Blažević, D. C. Carroll, K. Flippo, D. C. Gautier, M. Geibel, K. Harres, B. M. Hegelich, O. Lundh, K. Markey, P. McKenna, D. Neely, J. Schreiber, and M. Roth. Radiochromic film imaging spectroscopy of laser-accelerated proton beams. *Review of Scientific Instruments*, 80(2009), 2009.

[17] M. M. Guenther, A. Britz, R. J. Clarke, K. Harres, G. Hoffmeister, F. Nürnberg, A. Otten, A. Pelka, M. Roth, and K. Vogt. NAIS: Nuclear activation-based imaging spectroscopy. *Review of Scientific Instruments*, 84(7), 2013.

[18] J. S. Green, M. Borghesi, C. M. Brenner, D. C. Carroll, N. P. Dover, P. S. Foster, P. Gallegos, S. Green, D. Kirby, K. J. Kirkby, P. McKenna, M. J. Merchant, Z. Najmudin, C. A. J. Palmer, D. Parker, R. Prasad, K. E. Quinn, P. P. Rajeev, M. P. Read, L. Romagnani, J. Schreiber, M. J. V. Streeter, O. Tresca, C.-G. Wahlström, M. Zepf, and David Neely. Scintillator-based ion beam

profiler for diagnosing laser-accelerated ion beams. *Proc. of SPIE*, 8079:807919, 2011.

[19] J. Metzkes, L. Karsch, S. D. Kraft, J. Pawelke, and C. Richter, M. Schrer, M. Sobiella, N. Stiller, K. Zeil, and U. Schramm. A scintillator-based online detector for the angularly resolved measurement of laser-accelerated proton spectra. *Review of Scientific Instruments*, 83 (123301), 2012.

[20] M. J. Berger, J. S. Coursey, M. A. Zucker, and J. Chang. ESTAR, PSTAR, and ASTAR: Computer Programs for Calculating Stopping-Power and Range Tables for Electrons, Protons, and Helium Ions. *http://physics.nist.gov/Star [2016, April 15]*. National Institute of Standards and Technology, Gaithersburg, MD.

[21] J. B. Birks. *Theory and Practice of Scintillation Counting*. Pergamon, New York, 1964.

[22] K. Zeil, S. D. Kraft, S.Bock, M. Bussmann, T. E. Cowan, T. Kluge, J. Metzkes, T. Richter, R. Sauerbrey, and U. Schramm. The scaling of proton energies in ultrashort pulse laser plasma acceleration. *New Journal of Physics*, 12(4):045015, 2010.